Hindawi
Advances in Civil Engineering
Volume 2021, Article ID 6620058, 17 pages
https://doi.org/10.1155/2021/6620058

Research Article

Frost Resistance of Desert Sand Concrete

Haifeng Liu,[1,2] **Yingchang Ma**,[1] **Jurong Ma**,[2] **Weiwu Yang**,[1] **and Jialing Che**[1]

[1]*College of Civil and Hydraulic Engineering, Ningxia University, Yinchuan 750021, China*
[2]*Xinhuan College, Ningxia University, Yinchuan 750021, China*

Correspondence should be addressed to Haifeng Liu; liuhaifeng1557@163.com

Received 29 October 2020; Revised 16 March 2021; Accepted 22 March 2021; Published 30 March 2021

Academic Editor: Aboelkasim Diab

Demand for medium sand has increased greatly with increasing infrastructure construction items. The shortage of construction sand resources has become a serious problem in many districts. It not only increases the engineering cost, and the overexploitation of river sand and mountain as medium sand also brings a series of serious environment problems. There are abundant desert sand (DS) resources in western China. If DS resources can be used to substitute medium sand to produce desert sand concrete (DSC), which was suitable for engineering practice, the environment can be improved and engineering cost can be reduced. Although many researchers had focused on the mechanical performance of DSC, there were few documents on the frost resistance of DSC. Frost resistance experiments of DSC with 50% desert sand replacement ratio (DSRR) and ordinary concrete (OC) were performed in this paper. Influence of freeze-thaw cycles on the mechanical properties of OC and DSC was analyzed. Experimental results showed that, with increasing freeze-thaw cycles, the damage, peak strain, and porosity increased, while elastic modulus, Poisson's ratio, and peak stress declined, the stress-strain curves tended to be flat. Under the same condition of freeze-thaw cycles, the frost resistance of DSC with 50% DSRR was higher than that of OC. Constitutive model of DSC after different freeze-thaw cycles was formulated. The results predicted by constitutive model agreed well with experimental results, which can provide technical support for DSC engineering practice.

1. Introduction

As an indispensable raw material, medium sand is used to fill the gaps between coarse aggregates to enhance the concrete strength and compactability. Natural sand and machine-made sand are the main sources of medium sand but the overexploitation of which has seriously destroyed surrounding environment [1–3]. To reduce engineering cost and protect environment, it is essential to find alternative material to replace medium sand. 20% total land area of the earth is occupied by desert area. In China, the desert area is about 8% of the total land area. If the DS resource can be used to produce DSC suitable for practice, it will be very beneficial to construction projects and ecological environment. However, current researches indicated that the DS diameter and fineness modulus were far less than those of normal medium sand [4–8]. Fineness modulus of DS from Tengger desert and Mu Us sandy land in China are 0.334 and 0.194, respectively [4]. With the development of concrete technology and utility of highly effective water reducing agent, it is possible to use DS resources to produce DSC.

Currently, many researchers have focused on DSC mechanical properties. Zhang [4] researched the mechanical behaviors of DSC and desert sand mortar, in which the DS was obtained from Mu Us sandy land and Tengger desert. Fu et al. [5] studied DSC mechanical performance with 0.5 water-cement ratio and the range of sand-cement ratio was from 0.91 to 2.28. Experimental results showed that when sand-cement ratio was less than 1.14, the DSC strength was significantly higher than that of OC. Al-Harthy et al. [6] studied the mechanical properties of dune sand concrete with DSRR from 10% to 100%. DSC compressive strength decreased with the increase of DSRR, and the maximum decrease rate was less than 25%. Jin [7] studied DSC mechanical properties, which showed that DS can replace fine aggregate in concrete and the strength and performance can meet general engineering requirements. Zhang et al. [8] used universal testing machine to research the DSC dynamic

compressive strength and rupture strength after various temperatures. Liu et al. [9] used Split Hopkinson pressure bar to study DSC dynamic mechanical behavior; the influence of DSRR and strain rate on DSC dynamic mechanical behavior was analyzed. Mechanical behaviors of DSC after elevated temperature also were studied [10, 11].

Many parts in the world are located on cold zone with the long winter and large temperature difference between day and night. The freeze-thaw cycle was one of main factors, which can affect concrete durability [12]. Wang and Niu [13] investigated the effect of freeze-thaw cycles and sulfate corrosion resistance on mass loss rate and mechanical properties of shotcrete. Mcisaac and Fam [14] studied the influence of freeze-thaw cycles on the flexural performance of reinforced concrete beams. Bogas et al. [15] used recycled fine aggregate with the replacement rate of 0%, 20%, 50%, and 100% to replace natural fine aggregate and studied the mass loss rate and compressive strength after various freeze-thaw cycles. Alsaif et al. [16] studied surface scaling, internal damage, and mechanical performance of steel fibre-reinforced rubberized concretes with different freeze-thaw cycles. The steel fibre-reinforced rubberized concrete did not appear internal damage or degradation of mechanical properties after 56 freeze-thaw cycles. Research results indicated that the rubberized concrete can be used under freeze-thaw conditions. Richardson et al. [17] researched freeze-thaw durability of recycled aggregate concrete. Experimental results showed that the durability of recycled aggregate concrete was similar to virgin aggregate concrete. Penttala and Al-Neshawy [18] analyzed pore water pressure, stress, and strain of air-entrained concrete under the condition of freezing and thawing cycles by using theory analysis and experimental research. Yu et al. [19] used dynamic elastic modulus to define damage variable and establish damage fatigue equation to predict concrete service life under the action of repeated freezing and thawing. Failure mechanism of concrete under the action of freeze-thaw also was analyzed [20–23], which indicated that the freezing and expansion of pore water and the migration of free water in concrete will cause various pressures. When the pressure exceeded concrete tensile strength, new microcracks would be nucleated. The interaction between these new microcracks and the old microcracks eventually led to the fracture. Ma et al. [24] carried out cubic compressive strength test of concrete with single DS, single fly ash, and concrete mixed with DS and fly ash. The influence of DSRR and fly ash replacement ratio (FASR) on cubic compressive strength of concrete under low temperatures and after low temperatures was analyzed. Research results indicated that the DSC compressive strength increased firstly and then decreased with increasing DSRR. The compressive strength of DSC with DSRR of 50% was maximum value. Compressive strength of concrete mixed with DS and fly ash increased with the decrease of temperature under low temperature. The compressive strength of concrete mixed with DS and fly ash reached maximum value when DSRR and FASR were 50% and 10%.

Although many researchers had focused on the mechanical performance of DSC, there were few documents on the frost resistance of DSC. In this paper, on the basis of former researches, the frost resistance experiment of OC and DSC with DSRR of 50% was performed to study the effect of freeze-thaw cycles on DSC frost resistance. The pore structure of OC and DSC with DSRR of 50% after various freeze-thaw cycles was analyzed on the basis of stereology principles, which can provide theoretical support for performance evaluation of DSC in cold environment.

2. Experimental Scheme

P.O 42.5R Portland cement was used, and the basic performance indexes are listed in Table 1. Coarse aggregate was composed of local large stones and small stones. Particle size of large stones and small stones was 10~20 mm and 5~10 mm, respectively, and the mass ratio was 7 : 3. The fine aggregate included local artificial washed sand and DS. Appearance characteristics of fine aggregate are shown in Figure 1. DS was brought from Mu Us sandy land. The physical index and chemical composition of fine aggregate are listed in Tables 2 and 3. The gradation curves of all raw materials are shown in Figure 2. The polycarboxylic acid superplasticizer was used to ensure DSC workability.

Based on previous researches on the mechanical properties of DSC [24], prismatic concrete specimens with DSRR of 0% and 50% were further prepared for freeze-thaw test. Nine prismatic concrete specimens with the size of 100 mm × 100 mm × 300 mm were produce under each freeze-thaw cycle. The axial compressive strength, elastic modulus, and pore structure of concrete after freeze-thaw cycle were tested, and there were totally 108 prismatic specimens. The mix proportion of DSC is listed in Table 4.

2.1. Freeze-Thaw Test. The freeze-thaw experiment of DSC was performed according to Chinese Standard GB/T 50082-2009 [25]. TDR-28 rapid freeze-thaw testing machine, which was produced by the Tianjin Gangyuan test instrument factory, was used to carry out the freeze-thaw cycle test. After 24 d curing in standard curing room, DSC specimens were immersed into water with temperature of 20 ± 2°C for 4 d to reach water saturation. The specimens were taken out from water and wiped off. Initial ultrasonic propagation speed in specimen was determined rapidly. Then, DSC specimens were put into rubber specimen box with the dimension of 115 mm × 115 mm × 500 mm, which was surrounded by freeze-thaw medium in the freeze-thaw testing machine. The freeze-thaw medium in our test was tap water. The controlled temperature in central specimen was from −18 ± 2°C to 5 ± 2°C. Every freeze-thaw cycle was controlled for 4h. The temperature control curve of rapid freeze-thaw test is shown in Figure 3. Six designed freeze-thaw cycle times were 0, 25, 50, 75, 100, and 125, respectively. When the freeze-thaw cycle times were reached, the DSC specimens were taken out from rubber specimen box, and ultrasonic propagation speed was tested.

2.2. Ultrasonic Test. The DJUS-05 nonmetallic ultrasonic comprehensive detector was used to test ultrasonic wave

Table 1: Basic performance indexes of cement.

Cement setting time (min)		Rupture strength (MPa)		Compressive strength (MPa)		Fineness (%)	Ignition loss (%)	MgO (%)	SO_3 (%)
Initial time	Final time	3 d	28 d	3d	28 d	5.0	3.88	1.82	3.02
142	198	5.8	7.9	28.2	52.7				

(a) (b) (c)

Figure 1: Appearance characteristics of fine aggregate. (a) Artificial washing sand. (b) DS. (c) DS (50×).

Table 2: Physical index of fine aggregate.

Material	Fineness modulus	Bulk density ($g{\cdot}cm^{-3}$)	Apparent density ($g{\cdot}cm^{-3}$)	Sediment percentage (%)
Artificial washed sand	3.43	1.55	2.54	0.72
DS	0.24	1.40	2.62	0.14

Table 3: Chemical composition of fine aggregate.

Material	SiO_2 (%)	FeO (%)	Al_2O_3 (%)	CaO (%)	MgO (%)	K_2O (%)	Na_2O (%)	Loss on ignition (%)
Artificial washed sand	86.65	1.08	9.85	1.20	1.19	-	-	-
DS	82.66	1.85	8.72	2.00	1.51	0.12	0.07	0.49

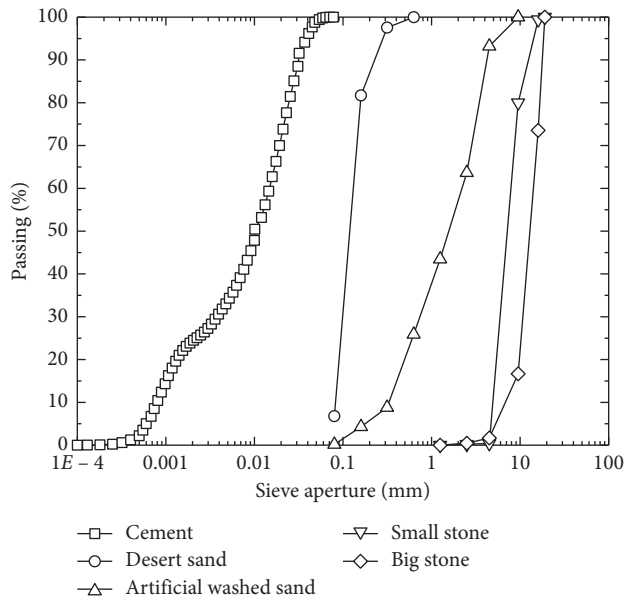

Figure 2: Gradation curves of raw materials.

propagation speed. According to Chinese Standard CECS-02:2005 [26], emission voltage, sampling period, and length were 250 V, 0.20 μs, and 512 mm, respectively. Test points and converter were evenly painted with Vaseline to achieve good coupling effect. The schematic diagram of test is shown in Figure 4. Five groups of test points were measured on opposite sides. Every test point was measured three times, and the average value was used as ultrasonic wave propagation speed for the test point. The average value of five test points was defined as ultrasonic wave propagation speed for the specimen, which was calculated in the following equation:

$$V_D = \frac{1}{5}\sum_{i=1}^{5} v_i, \quad (1)$$

where v_i was ultrasonic wave propagation speed in every test point.

2.3. Compressive Strength Experiment. Electronic universal testing machine was used to carry out compressive strength test, and its maximum load and accuracy were 1000 kN and

Table 4: Mix proportion of DSC.

No	DSRR (%)	Material consumption per unit volume (kg·m^{-3})						
		Water	Cement	Fly ash	Artificial sand	Desert sand	Large stone	Small stone
F01	0	195	390	0	635	0	826	354
F04	50	195	390	0	317	318	826	354

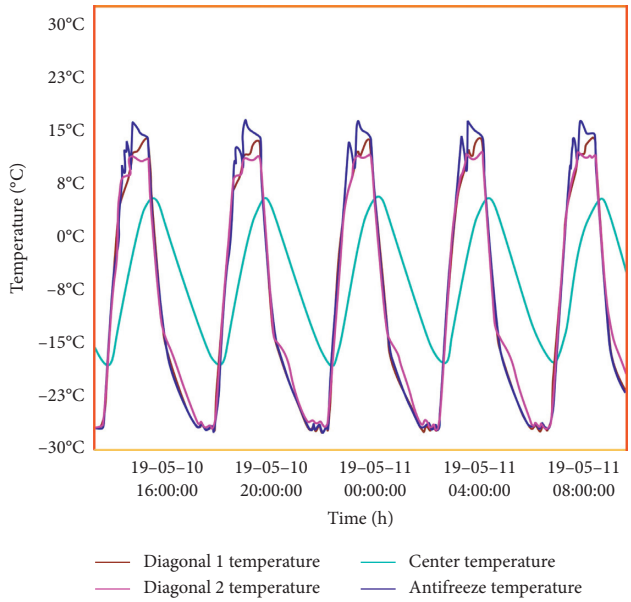

Figure 3: Temperature control curve of rapid freeze-thaw test.

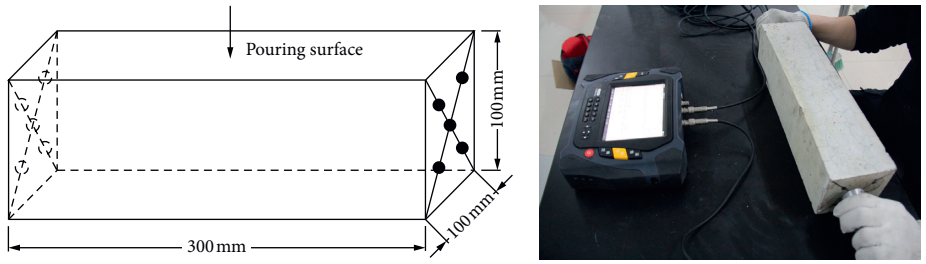

Figure 4: Ultrasonic test. (a) Schematic diagram of ultrasonic testing. (b) Actual diagram of ultrasonic testing.

0.001 N, respectively. The DH3820 high-speed static strain test system was adopted to collect experimental data. Sampling frequency, resolution ratio, and measurement range of strain were 10 Hz, ±50000 $\mu\varepsilon$, and 0.5 $\mu\varepsilon$, respectively. Linear variable differential transformers were used to detect compressive strain. Loading device of compressive strength test is plotted in Figure 5. Sensitivity coefficient, test range, and accuracy of LDVT were 2.00, 50 mm, and 500 $\mu\varepsilon$/mm, respectively.

After the rapid freeze-thaw test, the surfaces of DSC specimens became coarser, which was not conducive to stick strain gauge. Epoxy resin was painted on specimen surface to obtain flat surface. The electric resistance of strain gauge was 120 Ω. The length of axial strain gauge and transverse strain gauge was 100 mm and 50 mm and they were placed with a shape of "+."

According to Chinese Standard GB/T 50081-2002 [27], the compressive strength and elastic modulus were obtained with loading rate of 0.5 MPa/s. Before formal loading, preloads were performed up to 30% compression strength three times. The compressive strength of DSC was obtained by the following equation:

$$f_c = \frac{F}{A}, \tag{2}$$

where f_c is the DSC compressive strength, MPa; F is the specimen failure load, N; and A is the loading area, mm^2.

The elastic modulus was calculated as follows:

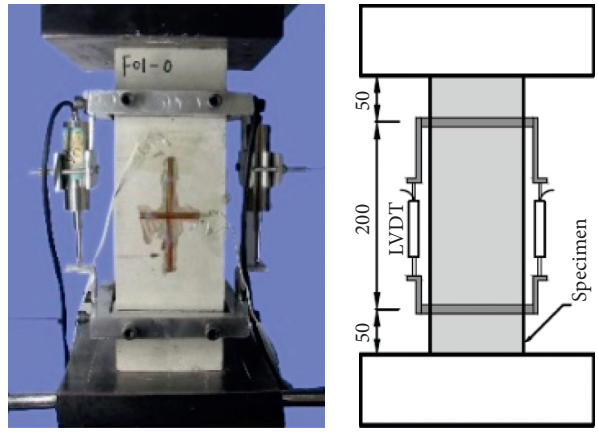

(a) (b)

Figure 5: Loading device of compressive strength test. (a) Actual loading map of test. (b) Loading sketch map of test.

$$E_c = \frac{F_a - F_0}{A} \times \frac{L}{\Delta n}, \tag{3}$$

where E_c is the elastic modulus, MPa; F_a is the loading when cross section stress was one third peak stress, N; F_0 is the initial loading when cross section stress was 0.5 MPa; L is the measurement distance of gauge, mm; and Δn is the deformation difference on both sides of specimen when the loading was applied from F_0 to F_a.

3. Results and Analysis

3.1. Failure Characteristics. Failure characteristics of unfrozen OC F01 at different loading stages are shown in Figure 6. At the beginning of loading, the cracking of prismatic specimens was hardly observed. As loading gradually increased, some tiny vertical cracks can be found on specimen surface. When the loading arrived at 0.8~0.9f_c, the dimension of longitudinal cracks gradually increased. The transverse cracks of concrete specimen also were nucleated and stretched. When axial loading approached to peak stress, the dimension of the cracks increased rapidly, which were accompanied with splitting sounds. After f_c, macrocracks gradually appeared on the specimen surface. Slabbing occurred on the middle part of specimen surface.

Figures 7 and 8 show the typical failure pictures of OC F01 and DSC F04 under different freeze-thaw cycles. With increasing freeze-thaw cycles, the specimen became looser. Different freeze-thaw cycles caused various microdamages such as holes, cracks, and looseness on the specimen surface [28]. For the same freeze-thaw cycles, the plastic deformation of DSC specimen F04 was larger than that of OC. OC specimen was far looser than DSC specimen F04. So, the failure of OC specimen was worse than that of DSC specimen F04.

3.2. Damage Variable. Ultrasonic wave propagation speed was an important index to symbol damage, and it was frequently used to determinate internal damage of concrete specimen [29, 30]. Damage D_n variable of concrete was defined by the following equation [31]:

$$D_n = 1 - \frac{V_D^2}{V_0^2}, \quad (0 \le D_n \le 1), \tag{4}$$

where V_0 and V_D are the ultrasonic propagation speed of concrete specimen before and after freeze-thaw cycles.

Figure 9 shows that Damage D_n increased with increasing freeze-thaw cycles. Under the freeze-thaw cycles of 25, 50, 75, 100, and 125 times, D_n of OC was 0.09, 0.14, 0.22, 0.27, and 0.39. Whereas, D_n of DSC with DSRR of 50% was 0.07, 0.11, 0.16, 0.22, and 0.32, respectively. Damage D_n of DSC with DSRR of 50% was lower than that of OC, which showed that DS can improve frost resistance of concrete. The relation between D_n and freeze-thaw cycles conformed to exponential function, which were shown in equations (5) and (6).

$$\text{OC} \quad D_n = 0.727 \times e^{(n/305.59)} - 0.716, \quad R^2 = 0.924, \tag{5}$$

$$\text{DSC with DSRR of 50\%} \quad D_n = 0.567 \times e^{(n/279.39)} - 0.566, \quad R^2 = 0.920. \tag{6}$$

Damage rate of OC and DSC after various freeze-thaw cycles was defined by the derivatives of equations (5) and (6). As shown in Figure 10, damage rate gradually increased with rising freeze-thaw cycles. For the same freeze-thaw cycles, the damage rate of DSC with DSRR of 50% was lower than that of OC.

3.3. Mechanical Properties. Peak stress σ_0, peak strain ε_0, elastic modulus E, and initial Poisson's ratio μ_0 of OC and DSC with DSRR of 50% are listed in Table 5.

3.3.1. Elastic Modulus. As shown in Figure 11, elastic modulus E decreases with increasing the freeze-thaw cycles. Compared with the elastic modulus of unfrozen OC, the

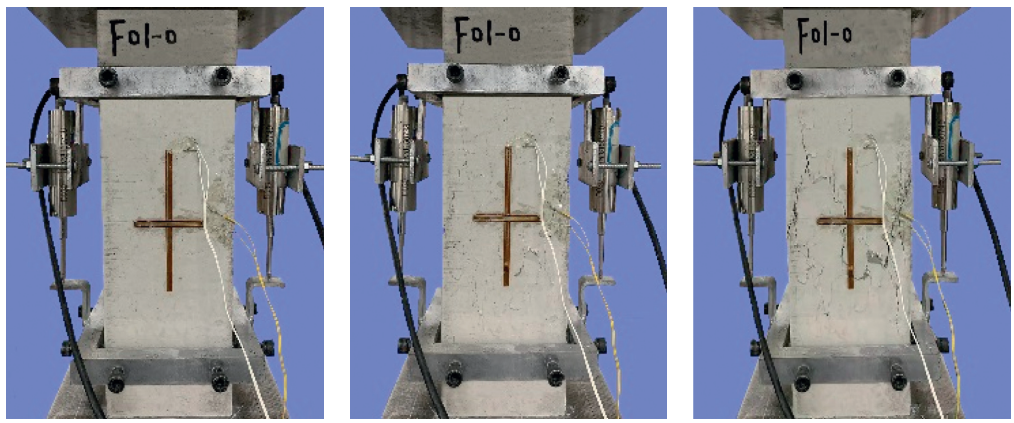

(a) (b) (c)

Figure 6: Failure pictures of OC F01 at different loading stages. (a) Initial loading. (b) 0.8~0.9f_c. (c) f_c.

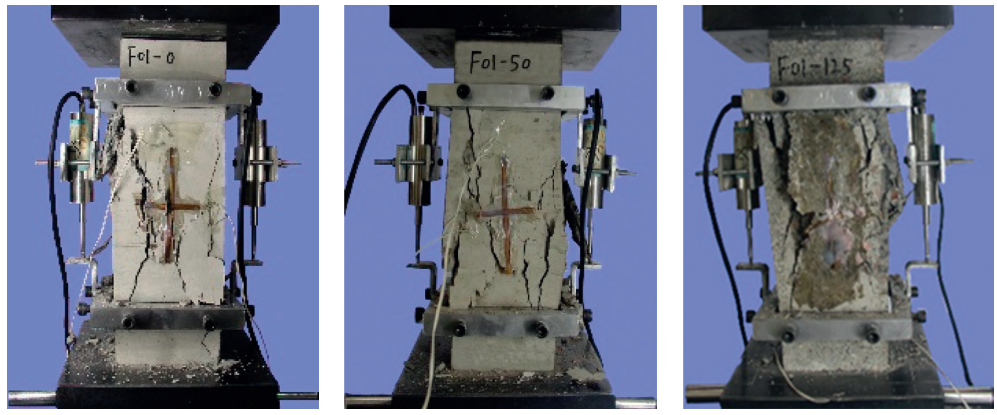

(a) (b) (c)

Figure 7: Typical failure pictures of OC specimen F01 under different freeze-thaw cycles. (a) 0 times. (b) 50 times. (c) 125 times.

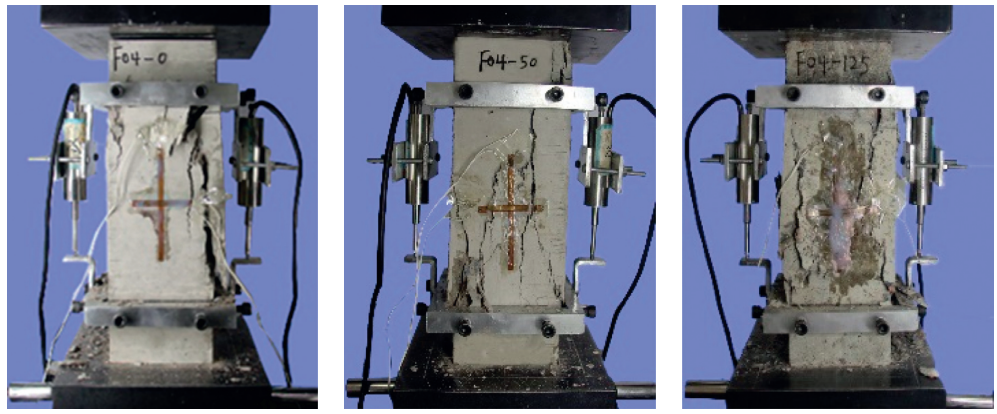

(a) (b) (c)

Figure 8: Typical failure pictures of DSC specimen F04 under different freeze-thaw cycles. (a) 0 times. (b) 50 times. (c) 125 times.

elastic modulus of OC decreased by 6.5%, 27.5%, 39.2%, 57.3%, and 69.6% under the freeze-thaw cycles of 25, 50, 75, 100, and 125 times, respectively. In comparison with elastic modulus of unfrozen DSC with 50% DSRR, the elastic modulus of DSC with 50% DSRR decreased by 5.1%, 21.7%, 34.8%, 51.4%, and 62.3%. So, for the same freeze-thaw cycles, the decrease in elastic modulus of OC was higher than that of DSC with 50% DSRR. At the same time, the elastic modulus

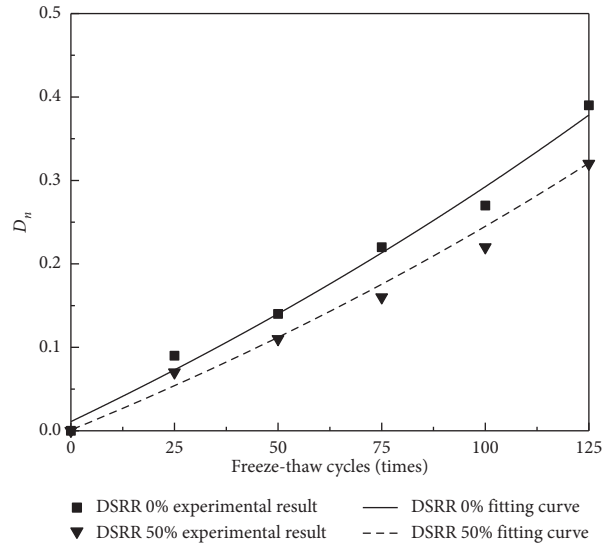

Figure 9: Relation between D_n and freeze-thaw cycles.

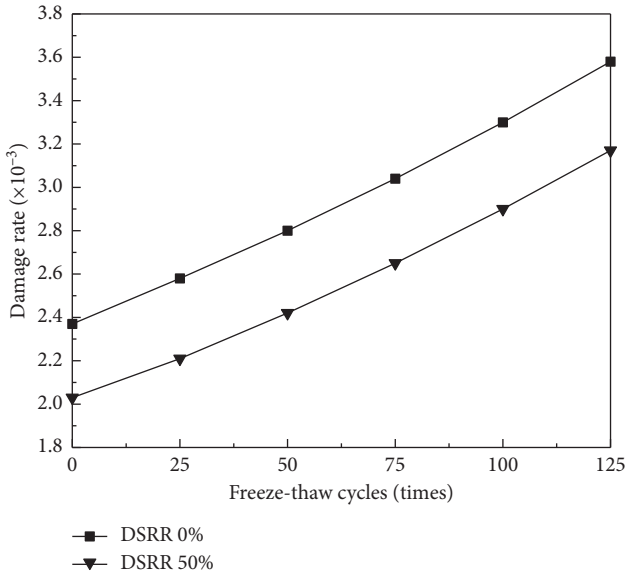

Figure 10: Relation between damage rate and freeze-thaw cycles.

Table 5: Mechanical properties of OC and DSC with 50% DSRR.

No	Index	Freeze-thaw cycles (times)					
		0	25	50	75	100	125
*F*01	σ_0 (MPa)	37.2	36.5	34.3	32.1	30.1	27.7
	ε_0 [$\times 10^{-3}$]	2.03	2.21	2.34	2.72	3.38	3.72
	E (MPa)	3.09×10^4	2.89×10^4	2.24×10^4	1.88×10^4	1.32×10^4	9.4×10^3
	μ_0	0.210	0.197	0.180	0.167	0.153	0.144
*F*04	σ_0 (MPa)	38.4	38.1	36.9	34.8	33.0	29.8
	ε_0 [$\times 10^{-3}$]	1.98	2.01	2.30	2.58	3.11	3.53
	E(MPa)	3.13×10^4	2.97×10^4	2.45×10^4	2.04×10^3	1.52×10^4	1.18×10^4
	μ_0	0.208	0.204	0.189	0.178	0.165	0.151

E of OC was lower than that of DSC with 50% DSRR. This may be caused by following reasons. On the one hand, when the specimen was frozen, the pore water in the concrete would expand. The internal damage of concrete began to accumulate and intensify after repeated freeze-thaw cycles [22, 23]. On the other hand, DS was considered as a kind of

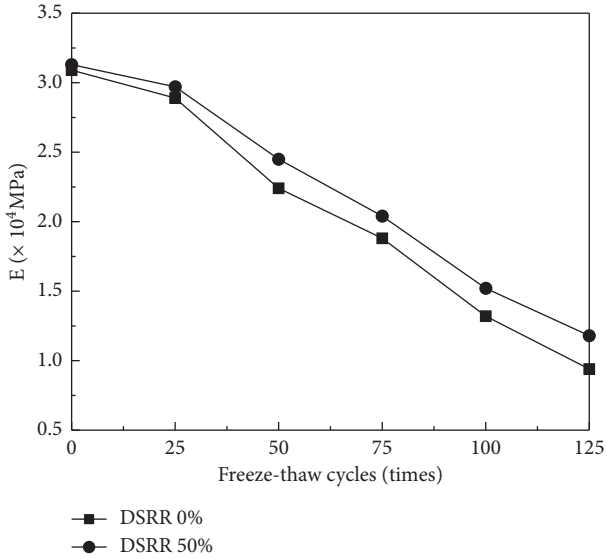

Figure 11: Relation between elastic modulus and freeze-thaw cycles.

mineral substance, which can further react with cement and improve mechanical performance of concrete in the process of freeze-thaw cycles [5, 32, 33].

3.3.2. Poisson's Ratio. Poisson's ratio was an important index to calculate engineering cracking and deformation of concrete. With increasing freeze-thaw cycles, initial Poisson's ratio u_0 decreased. Compared with initial Poisson's ratio of unfrozen OC, u_0 of OC decreased by 6.2%, 14.3%, 20.5%, 27%, and 31.4% under the freeze-thaw cycles of 25, 50, 75, 100, and 125 times, respectively. In comparison with Poisson's ratio of unfrozen DSC with 50% DSRR, Poisson's ratio u_0 of DSC with 50% DSRR decreased by 2%, 9.1%, 14.4%, 20.7%, and 27.4%. For the same freeze-thaw cycles, the decrease in u_0 of OC was higher than that of DSC with 50% DSRR. On the whole, u_0 of DSC with 50% DSRR was higher than that of OC.

As shown in Figure 12, when (σ/σ_0) was less than or equal to 0.6, the increase for the axial deformation of OC and DSC with 50% DSRR was larger than that in transverse deformation. Poisson's ratio $\boldsymbol{\mu}$ increased slowly. When (σ/σ_0) was more than 0.6, the increase for transverse deformation of OC and DSC with 50% DSRR was more rapidly than that in axial deformation. Poisson's ratio μ increased rapidly.

When (σ/σ_0) was equal to 0.4, the relation between Poisson's ratio and freeze-thaw cycles is shown in Figure 13. With the enhancement of freeze-thaw cycles, Poisson's ratio of OC and DSC with 50% DSRR declined gradually. Compared with Poisson's ratio of unfrozen OC, μ of OC decreased by 6%, 17%, 26%, 37%, and 43% under the freeze-thaw cycles of 25, 50, 75, 100, and 125 times, respectively. In comparison with Poisson's ratio of unfrozen DSC with 50% DSRR, μ of DSC with 50% DSRR decreased by 2%, 11%, 14%, 24%, and 37%. For the same freeze-thaw cycles, the decrease for Poisson's ratio of DSC with 50% DSRR was lower than that of OC, which was caused by good plastic deformation and little internal damage of DSC with 50% DSRR.

3.3.3. Peak Stress. As listed in Table 5, peak stress decreased with increasing freeze-thaw cycles. Compared with peak stress of unfrozen OC, the peak stress of OC decreased by 1.4%, 7.8%, 13.7%, 19.1%, and 25.5% under the freeze-thaw cycles of 25, 50, 75, 100, and 125 times, respectively. In comparison with peak stress of unfrozen DSC with 50% DSRR, the peak stress of DSC with 50% DSRR decreased by 0.8%, 3.9%, 9.4%, 14%, and 22.4%. So, the decrease in OC peak stress was higher than that in DSC with 50% DSRR. With the same freeze-thaw cycles, the peak stress of DSC with 50% DSRR was higher than that of OC, which may be caused by small size of DS. The size of DS was so small that the gaps between coarse aggregates were filled effectively to improve pore structure of DSC.

Figure 14 shows that the relative peak stress of OC and DSC with 50% DSRR decreased with the increase of freeze-thaw cycles. The relation between relative peak stress and freeze-thaw cycles was obtained by linear regression, which is shown in the following equations:

$$\text{OC} \quad \frac{\sigma_{CD}}{\sigma_{C0}} = -0.0021N + 1.0198, \quad R^2 = 0.979, \tag{7}$$

$$\text{DSC with DSRR of 50\%} \quad \frac{\sigma_{SD}}{\sigma_{S0}} = -0.0017 + 1.0261, \quad R^2 = 0.931, \tag{8}$$

where $\sigma_{C0}$and $\sigma_{S0}$are the peak stresses of unfrozen OC and DSC with 50% DSRR; $\sigma_{C\,D}$ and $\sigma_{S\,D}$ are the peak stresses of OC and DSC with 50% DSRR under different freeze-thaw cycles; and N is the freeze-thaw cycle.

Figure 15 shows that the relative peak stress of OC and DSC with 50% DSRR increased with the enhancement of relative ultrasonic wave propagation speed. The relation

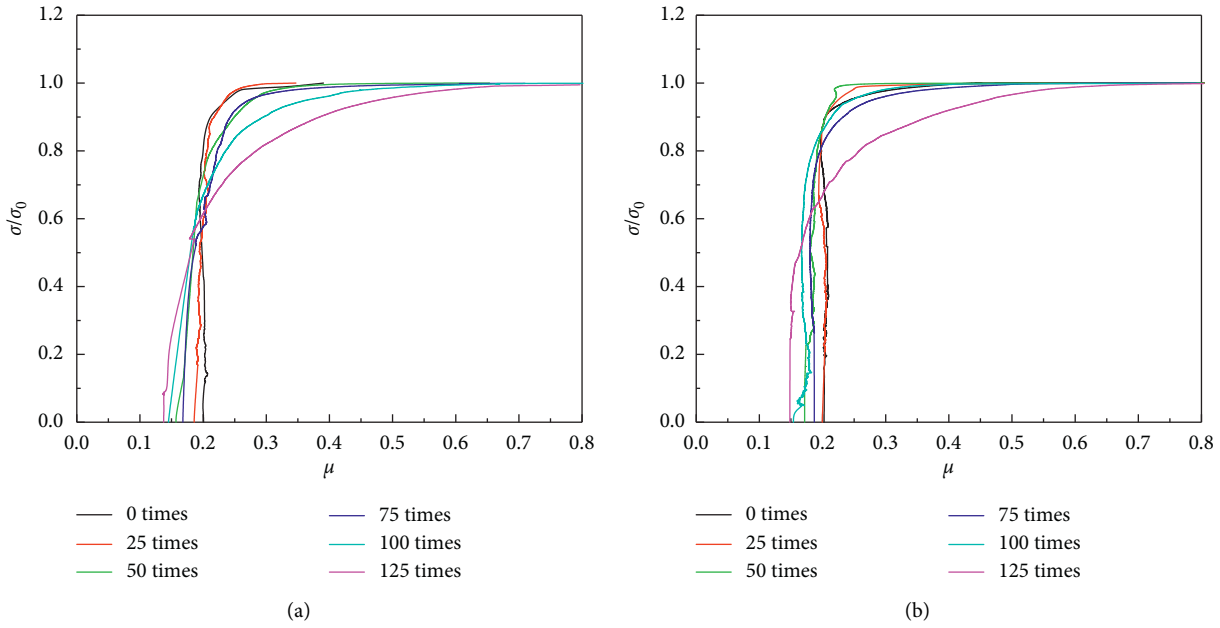

Figure 12: Relation between (σ/σ_0) and μ. (a) OC. (b) DSC with 50% DSRR.

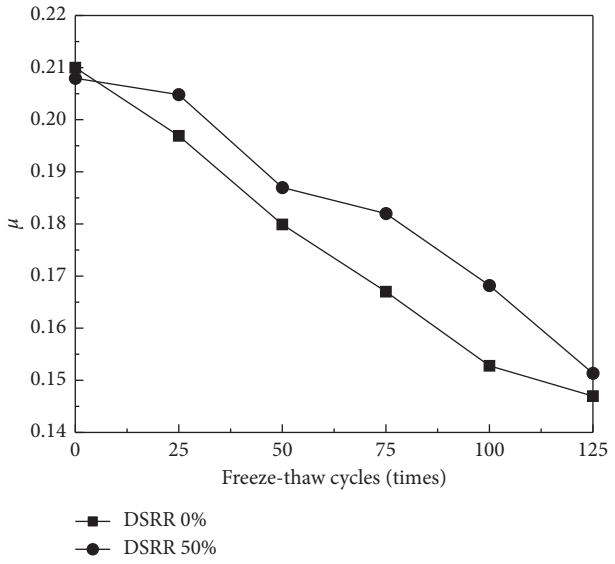

Figure 13: Relation between Poisson's ratio (σ/σ_0) and freeze-thaw cycles

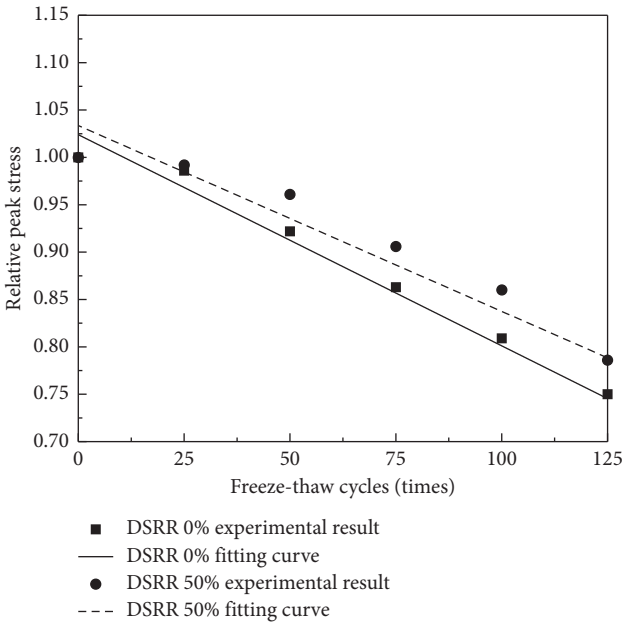

Figure 14: Relation between relative peak stress and freeze-thaw cycles.

between relative peak stress and relative ultrasonic wave propagation speed conformed to linear relation, which is shown in the following equations:

$$\text{OC} \quad \frac{\sigma_{CD}}{\sigma_{C0}} = 1.2590\frac{v_{CD}}{v_{C0}} - 0.2444, \quad R^2 = 0.965, \tag{9}$$

$$\text{DSC with DSRR of 50\%} \quad \frac{\sigma_{SD}}{\sigma_{S0}} = 1.3106\frac{v_{SD}}{v_{S0}} - 0.2918, \quad R^2 = 0.966, \tag{10}$$

where v_{C0} and v_{S0} are the ultrasonic wave propagation speed of unfrozen OC and DSC with DSRR of 50% and v_{CD} and v_{SD} are the ultrasonic propagation speed of OC and DSC with DSRR of 50% under different freeze-thaw cycles.

3.3.4. Peak Strain. Peak strain is the strain which corresponds to peak stress. As listed in Table 5, peak strain ε_0 increased with freeze-thaw cycles. Compared with peak strain of unfrozen OC, the peak strain ε_0 of OC increased by

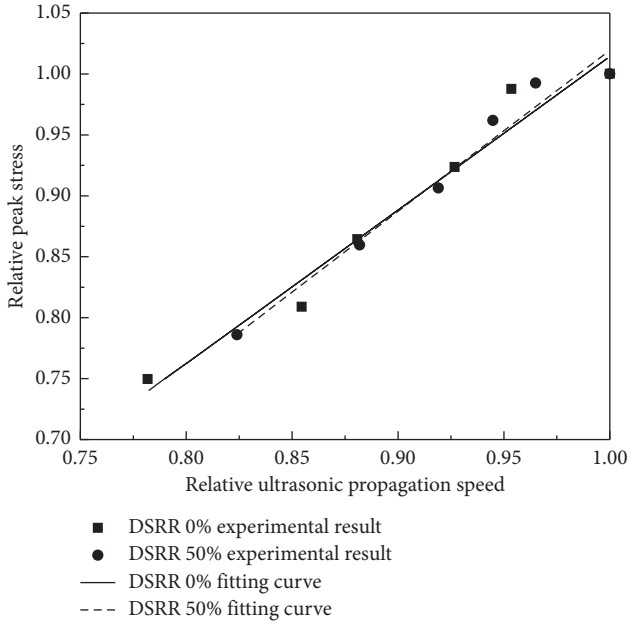

Figure 15: Relation between relative peak stress and relative ultrasonic propagation speed.

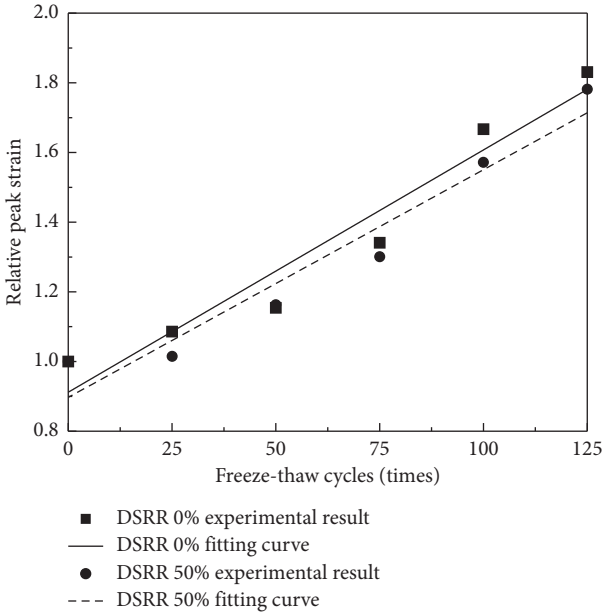

Figure 16: Relation between relative peak strain and freeze-thaw cycles.

8.9%, 15.3%, 34%, 66.5%, and 83.3% under the freeze-thaw cycles of 25, 50, 75, 100, and 125 times, respectively. In comparison with peak strain of unfrozen DSC with 50% DSRR, the peak strain ε_0 of DSC with 50% DSRR increased by 1.5%, 16.2%, 30.3%, 57.1%, and 78.3%. So, the increase of OC peak strain was higher than that of DSC with 50% DSRR. For the same freeze-thaw cycles, the peak strain ε_0 of DSC with 50% DSRR was lower than that of OC. This was because that DS effectively filled the gaps between coarse aggregates and formed a solid skeleton, which led to a reduction of DSC deformation.

Figure 16 shows that relative peak strain increased with increasing freeze-thaw cycles. The relation between relative peak strain and freeze-thaw cycles was obtained by linear regression, which is shown in the following equations:

$$\text{OC} \quad \frac{\varepsilon_{CD}}{\varepsilon_{C0}} = 0.0070N + 0.9119, \quad R^2 = 0.926, \tag{11}$$

$$\text{DSC with DSRR of 50\%} \quad \frac{\varepsilon_{SD}}{\varepsilon_{S0}} = 0.0065N + 0.8970, \quad R^2 = 0.927, \tag{12}$$

where ε_{C0} and ε_{S0} are the peak strains of unfrozen OC and DSC with 50% DSRR and ε_{CD} and ε_{SD} are the peak strains of OC and DSC with 50% DSRR under different freeze-thaw cycles.

3.4. Stress-Strain Curve. Figure 17 shows that, with the increase of freeze-thaw cycles, the stress-strain curves of OC and DSC with 50% DSRR gradually deviated from Y-axis direction and had a tendency to be flat.

As shown in Figure 18, the shape of stress-strain curve of DSC with 50% DSRR resembled to that of OC. At the initial stage, the stress was linear with strain and curve slope gradually decreased with increasing freeze-thaw cycles. For the same freeze-thaw cycles, the curve slope of DSC with 50% DSRR was larger than that of OC. As axial loading increased, the ascending part of stress-strain curve presented a concave phenomenon gradually. Compared with stress-strain curve of DSC with 50% DSRR, the concave phenomenon of OC was more obvious. As freeze-thaw cycle increased, the inner structure of specimen became loose and many microcracks were nucleated and stretched. Because the DS particle size was smaller than that of artificial washed sand (Figure 3), DS can greatly improve fine aggregate grain composition. The damage of OC was larger than that of DSC with 50% DSRR, and its concave phenomenon was more obvious under the condition of loading. As axial loading continued to increase, the growth rate of stress did not synchronize with that of strain and stress-strain curve was nonlinear. After loading to peak stress, stress decreased rapidly and deformation increased continuously.

3.5. Constitutive Model. The constitutive model of concrete was significant for theoretical analysis and structure design. Currently, many scholars have done enormous researches on constitutive model of concrete, such as Sargin [34], Hogenetad [35], and Guo [36]. The softening stage of stress-strain curve was not ideal due to the complexity of concrete composition. For simplicity, the constitutive model of concrete under axial compression was suggested by Guo [36] was used, which can be expressed as follows:

$$y = \begin{cases} Ax + (3 - 2A)x^2 + (A - 2)x^3, & 0 < x < 1, \\ x\left[a(x - 1)^2 + x\right]^{-1}, & x \geq 1, \end{cases} \tag{13}$$

where y $(= (\sigma/\sigma_0))$ and x $(= (\varepsilon/\varepsilon_0))$ are the nondimensional stress and strain, respectively; A is the initial tangent slope of

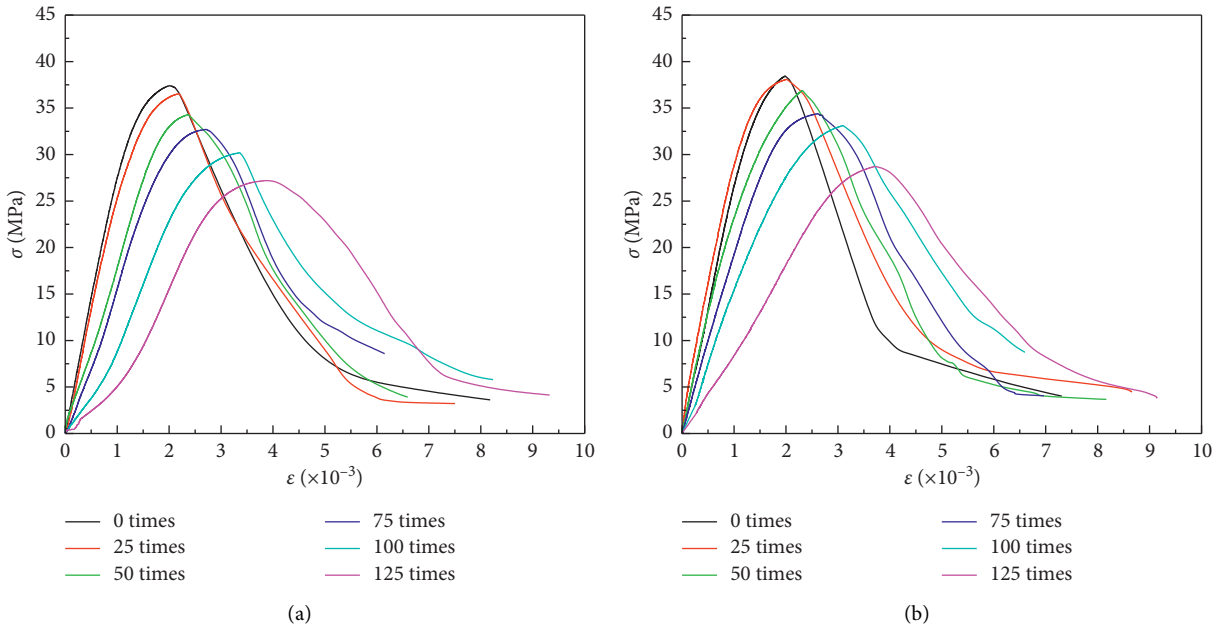

Figure 17: Stress-strain curve of OC and DSC with 50% DSRR under different freeze-thaw cycles. (a) OC. (b) DSC with 50% DSRR.

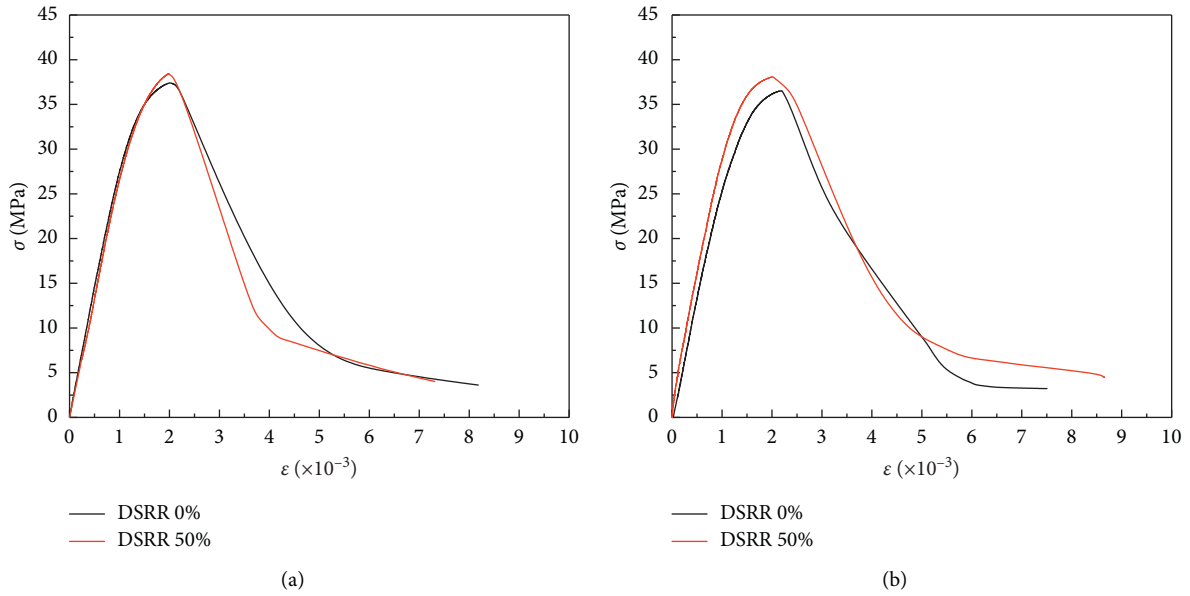

Figure 18: Continued.

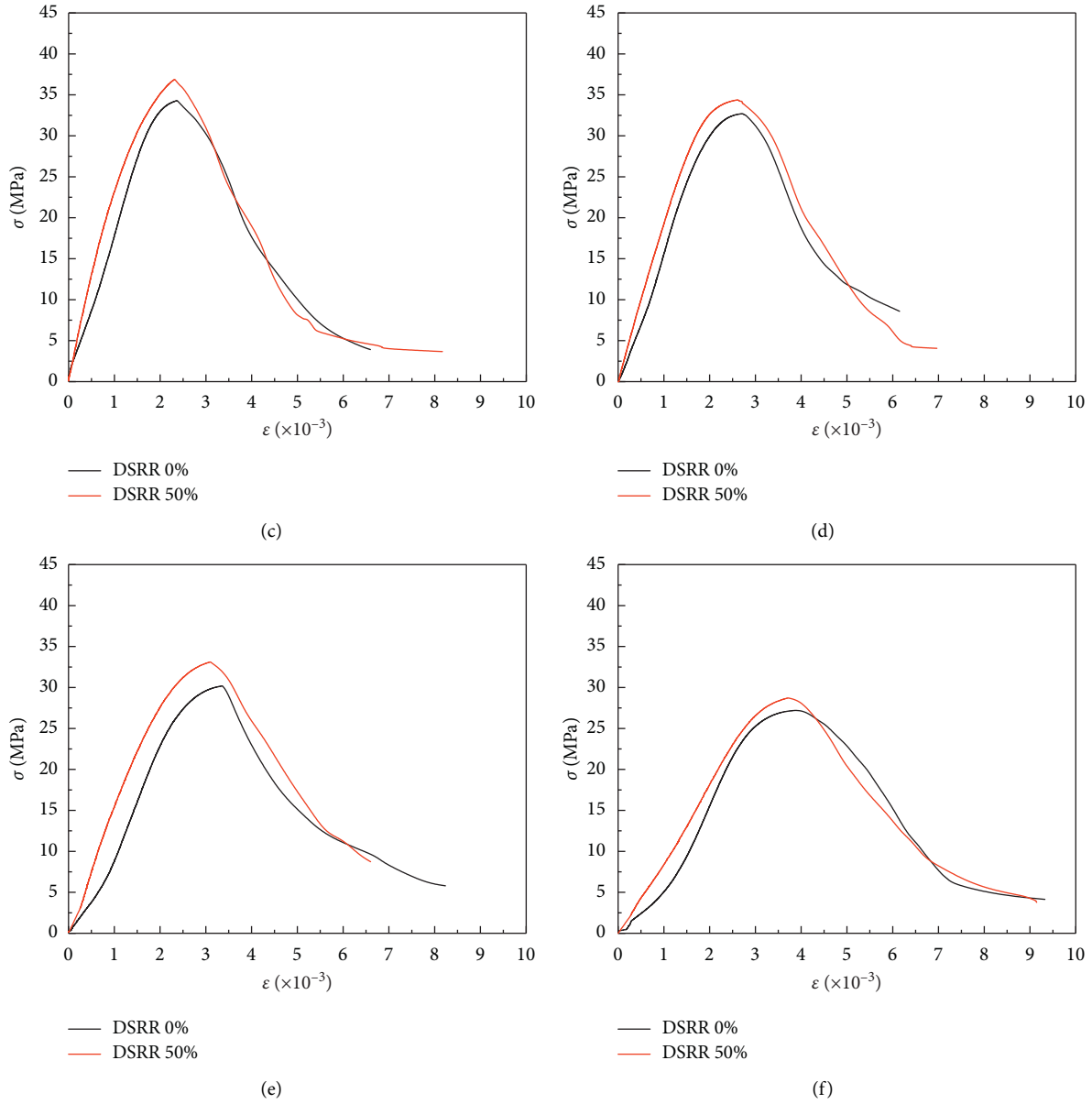

Figure 18: Comparison of stress-strain curves under different freeze-thaw cycles. (a) 0 times. (b) 25 times. (c) 50 times. (d) 75 times. (e) 100 times. (f) 125 times.

stress-strain curve; and a is the area under the softening stage of stress-strain curve.

Control parameter values A and a reflected plastic deformation capacity of concrete. The larger A and the smaller a, the smoother the curve, the larger plastic deformation, the higher residual strength, and the slower failure process [37]. The control parameter values A and a of OC and DSC with DSRR of 50% are listed in Table 6. With increasing freeze-thaw cycles, A decreased while a increased. At the same time, the plastic deformation and residual strength of OC and DSC with DSRR of 50% decreased.

Figure 19 shows that the ascending part of predicted curves agreed well with experimental curves. However, the soften parts differed from each other greatly. Correlation coefficients R^2 for ascending part and soften part were greater than 0.9. Therefore, the constitutive model of OC and DSC with 50% DSRR can be used to provide theory analysis and technical support.

4. Pore Structure

Based on stereology principles [38], stereological image analysis was adopted to measure and analyze pore structure of OC and DSC with 50% DSRR under different freeze-thaw cycles. Figure 20 shows that the porosity increased with increasing freeze-thaw cycles. Compared with porosity of unfrozen concrete, the porosity of OC increased by 0.79%, 2.24%, 4.10%, 6.21%, and 7.79% under the freeze-thaw cycles of 25, 50, 75, 100, and 125 times, respectively. In comparison with porosity of unfrozen DSC with 50% DSRR, the DSC porosity with 50% DSRR increased by 0.76%, 1.99%, 3.98%, 6.12%, and 7.65%.

Table 6: Parameters A and a of OC and DSC with 50% DSRR.

No			Freeze-thaw cycles (times)					
			0	25	50	75	100	125
Parameter	A	F01	1.810	1.810	1.120	1.270	0.800	0.250
		F04	1.790	1.840	1.600	1.520	1.490	0.400
	a	F01	3.350	3.370	3.580	4.220	3.840	3.840
		F04	2.860	2.120	3.650	3.520	3.740	3.810
Correlation coefficient R^2	A	F01	0.990	0.996	0.988	0.990	0.994	0.971
		F04	0.998	0.999	0.982	0.992	0.989	0.979
	a	F01	0.938	0.907	0.980	0.981	0.961	0.959
		F04	0.971	0.986	0.977	0.964	0.963	0.968

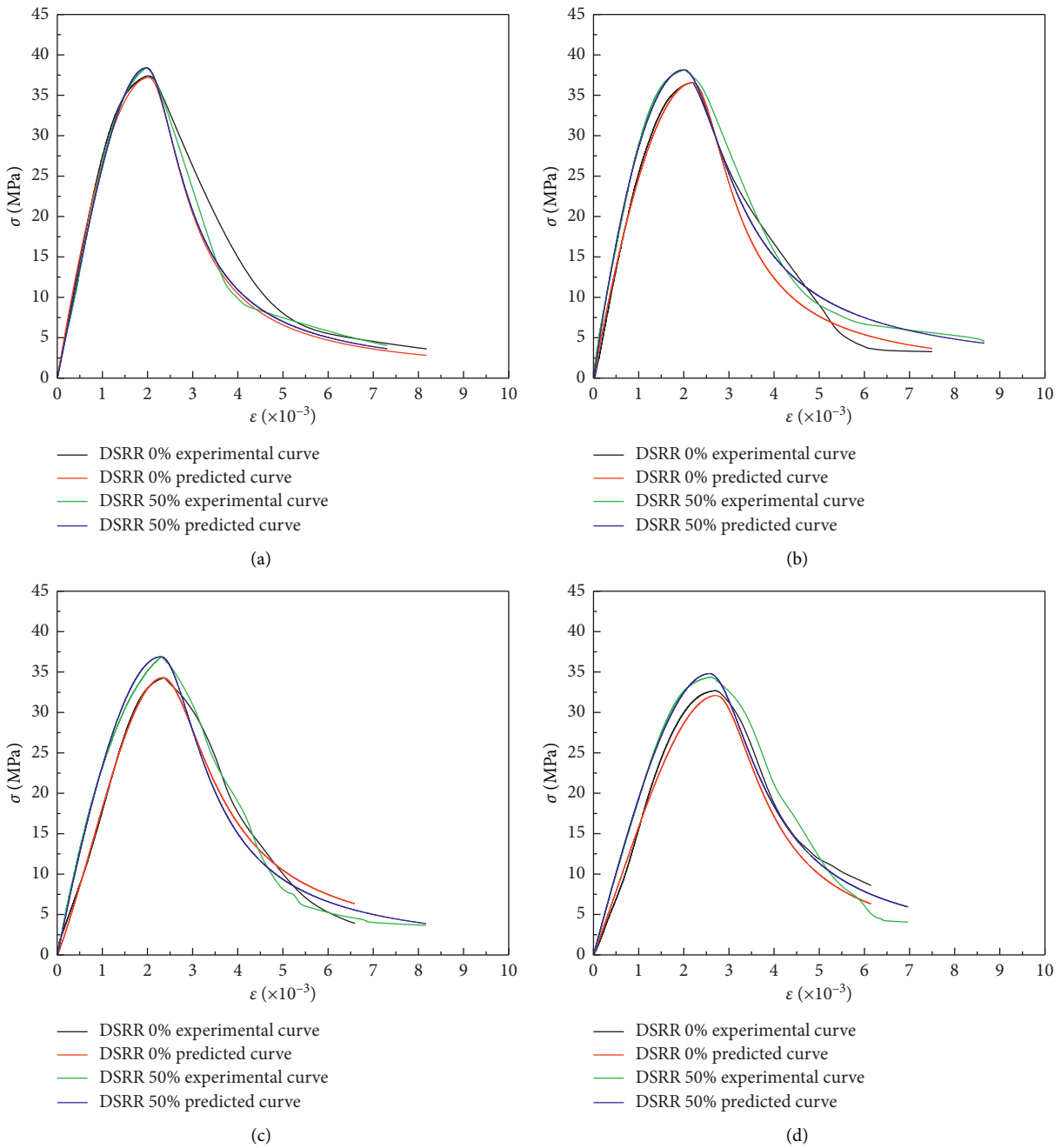

Figure 19: Continued.

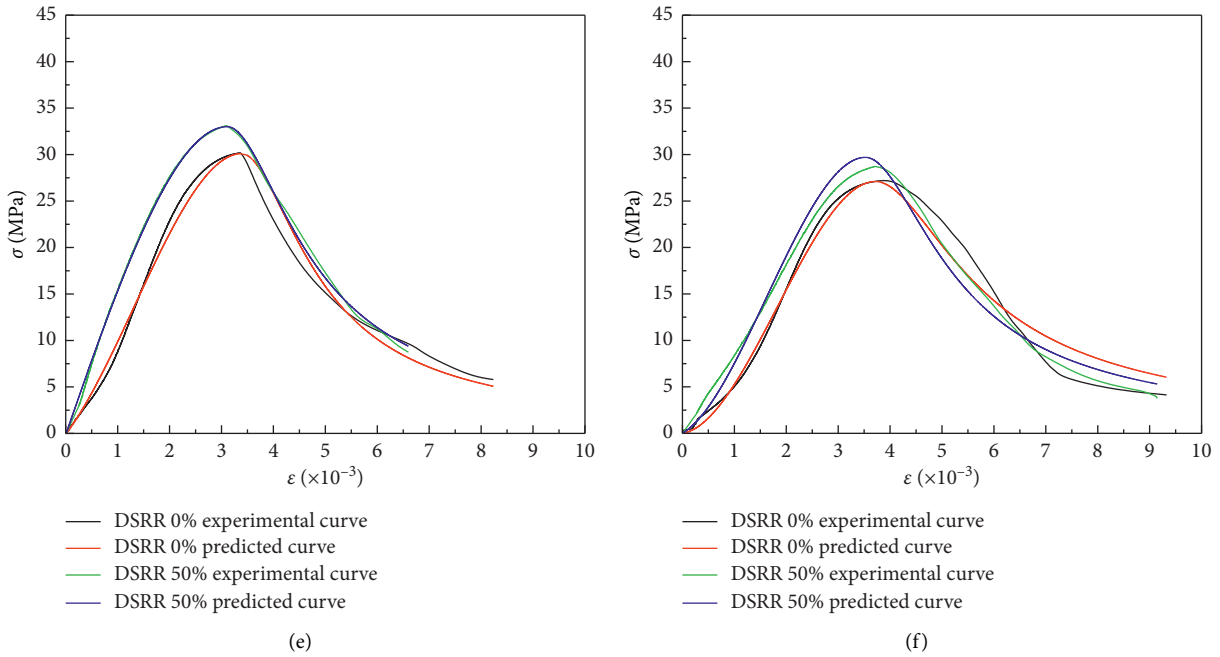

Figure 19: Comparison between predicted results and experimental results of OC and DSC with 50% DSRR under different freeze-thaw cycles. (a) 0 times. (b) 25 times. (c) 50 times. (d) 75 times. (e) 100 times. (f) 125 times.

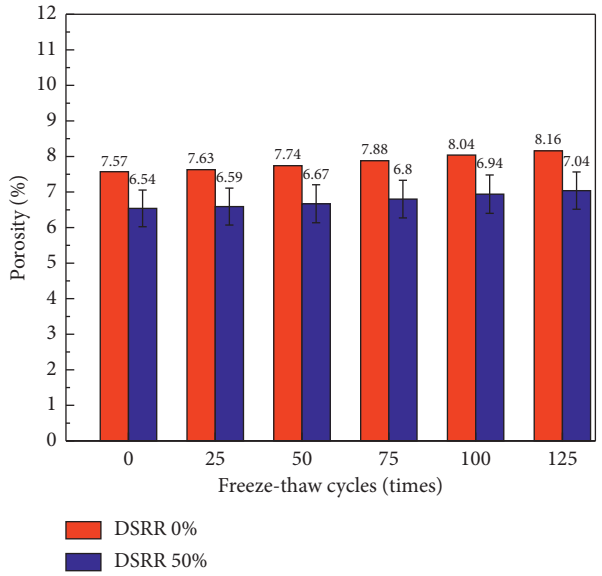

Figure 20: Porosity of OC and DSC with 50% DSRR under different freeze-thaw cycles.

For the same freeze-thaw cycles, the DSC porosity with 50% DSRR was lower than that of OC.

As shown in Figures 21 and 22, the DSC pore size distribution with 50% DSRR highly resembled to that of OC. The porosity with pore size ranging from 10 μm to 200 μm and larger than 2000 μm was higher than others. However, the porosity with pore size larger than 800 μm was lower than that ranging from 10 μm to 800 μm.

Figure 23 shows that the compressive strength of OC and DSC with 50% DSRR decreased with increasing porosity. The relation between compressive strength and porosity p was formulated by linear regressive analysis, which are shown in equations (14) and (15). Obviously, there was a good relation between porosity and compressive strength of OC and DSC with 50% DSRR:

$$\text{OC} \quad f_c = -13.71p + 142.09, \quad R^2 = 0.848, \tag{14}$$

$$\text{DSC with DSRR of 50\%} \quad f_c = -10.95p + 120.35, \quad R^2 = 0.898. \tag{15}$$

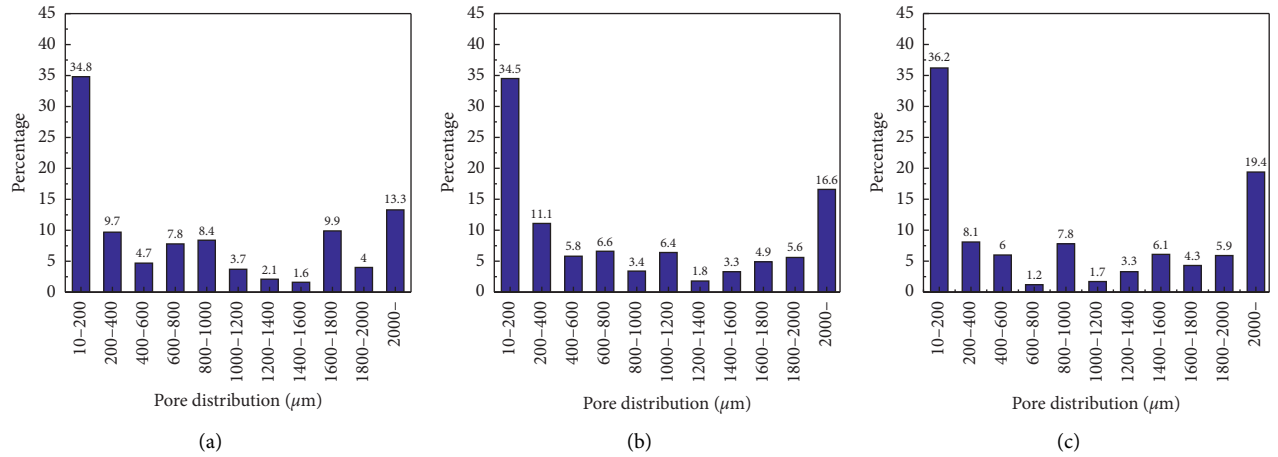

Figure 21: Pore size distribution of OC with different freeze-thaw cycles. (a) 0 times. (b) 50 times. (c) 125 times.

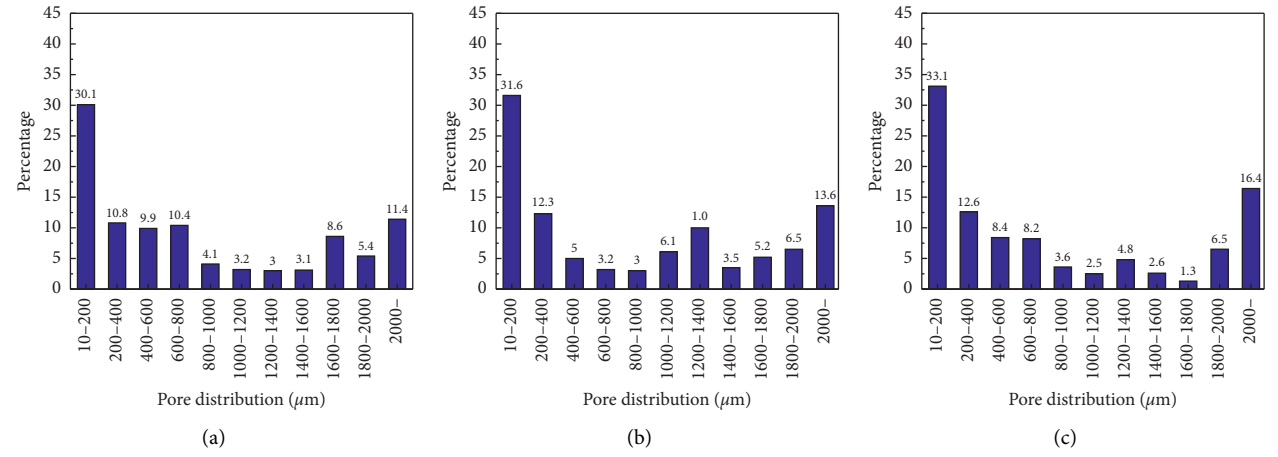

Figure 22: Pore size distribution of DSC with different freeze-thaw cycles. (a) 0 times. (b) 50 times. (c) 125 times.

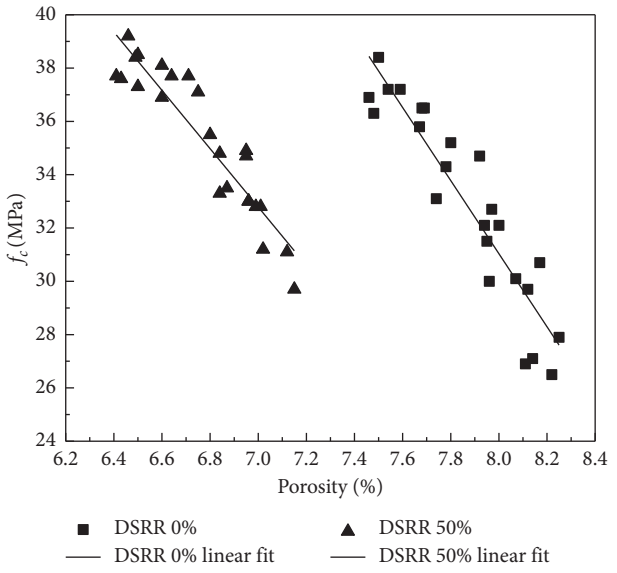

Figure 23: Relation between compressive strength and porosity.

5. Conclusions

In this paper, the frost resistance experiments of OC and DSC with DSRR of 50% were performed. The effect of freeze-thaw cycles on mechanical properties of OC and DSC with DSRR of 50% was analyzed. Experimental results can provide theoretical support for the DSC engineering application in cold district. Following conclusions were reached:

(1) The failure pattern of DSC with 50% DSRR resembled to that of OC. The structure of DSC and OC became looser with increasing freeze-thaw cycles. When the freeze-thaw cycle remained the same, the plastic deformation of DSC with 50% DSRR was larger than that of OC, and the failure process of DSC with 50% DSRR was slower than that of OC.

(2) The elastic modulus, Poisson's ratio, and peak stress declined, while damage and peak strain increased as freeze-thaw cycles increased. With the same freeze-thaw cycles, the frost resistance of DSC with 50% DSRR was better than that of OC.

(3) The stress-strain curve of DSC was similar to that of OC. With the increase of freeze-thaw cycles, stress-strain curves of DSC with 50% DSRR and OC gradually deviated from *Y*-axis direction and tended to be flat. The predicted results from the constitutive model agreed well with experimental results.

(4) The porosity of OC and DSC with 50% DSRR increased with increasing freeze-thaw cycles.

As mentioned above, the study on the frost resistance of OC and DSC with DSRR of 50% was carried out in this paper. In order to provide technical support for the utility of DSC in cold zone, the frost resistance of DSC with various DSRR should be further performed and optimal DSRR would be determined. At the same time, carbonization and chloride ion penetration performance should be researched in the future.

Data Availability

The data used to support this study are included within the article.

Conflicts of Interest

The authors declare no conflicts of interest.

Authors' Contributions

H.L. provided the idea and applied for funding to support this paper. Y.M. and J.M. performed these experiments. Y.M. contributed to the analysis of experiment data. Y.M. and H.L. wrote this paper. W.Y. and J.C. put forward opinions for this paper.

Acknowledgments

The support of the Science Foundation of Ningxia (2020AAC03044), the Scientific and Technological Research Project for Institutions of higher Learning in Ningxia of China ((NGY2020104)), the National Natural Science Foundation of China (Nos. 51368048 and 11162015) and the First class discipline construction in Ningxia colleges and Universities (Discipline of water conservancy engineering) (NXYLXK 2021A03) are gratefully acknowledged by the authors.

References

[1] D. J. Harrison and E. J. Steadman, "Alternative source of aggregates," British Geological Survey Commissioned Report, CR/03/95N, British Geological Survey, Nottingham, UK, 2003.

[2] M. Macfarlane and P. Mitchell, "Scoping and assessment of the environmental and social impacts of river mining in Jamaica," *Chemistry*, vol. 8, no. 21, pp. 4980–4991, 2003.

[3] O. H. Pilkey, R. S. Young, J. Kelley, and A. D. Griffith, *Mining of Coastal Sand: A Critical Environmental and Economic Problem for morocco*, White Paper, Western Carolina University, Cullowhee, NC, USA, 2007.

[4] G. Zhang, J. Song, J. Yang, and X. Liu, "Performance of mortar and concrete made with a fine aggregate of desert sand," *Building and Environment*, vol. 41, no. 11, pp. 1478–1481, 2006.

[5] J. L. Fu, H. Li, P. Zhu et al., "Effect of very fine particles on workability and strength of concrete made with dune sand," *Construction and Building Materials*, vol. 47, pp. 131–137, 2013.

[6] A. S. Al-Harthy, M. A. Halim, R. Taha, and K. S. Al-Jabri, "The properties of concrete made with fine dune sand," *Construction and Building Materials*, vol. 21, no. 8, pp. 1803–1808, 2007.

[7] B. H. Jin, J. X. Song, and H. F. Liu, "Engineering characteristics of concrete made of desert sand from Maowusu Sandy Land," *Applied Mechanics and Materials*, vol. 174–177, pp. 604–607, 2012.

[8] M. Zhang, H. Liu, S. Sun, X. Chen, and S. I. Doh, "Dynamic mechanical behaviors of desert sand concrete (DSC) after different temperatures," *Applied Sciences*, vol. 9, no. 19, pp. 4151–4169, 2019.

[9] H. Liu, J. Ma, Y. Wang, and J. Ning, "Influence of desert sand on the mechanical properties of concrete subjected to impact loading," *Acta Mechanica Solida Sinica*, vol. 30, pp. 583–595, 2017.

[10] H. Liu, X. Chen, J. Che, N. Liu, and M. Zhang, "Mechanical performances of concrete produced with desert sand after elevated temperature," *International Journal of Concrete Structures and Materials*, vol. 14, no. 26, pp. 1–15, 2020.

[11] H. F. Liu, J. R. Ma, Y. L. Chen, and D. Yang, "Mechanical properties of high strength desert sand concrete," *Advanced Materials Research*, vol. 1095, pp. 263–266, 2015.

[12] S. E. E. Khay, J. Neji, and A. Loulizi, "Compacted dune sand concrete for pavement applications," *Proceedings of the Institution of Civil Engineers - Construction Materials*, vol. 164, no. 2, pp. 87–93, 2011.

[13] J. Wang and D. Niu, "Influence of freeze-thaw cycles and sulfate corrosion resistance on shotcrete with and without steel fiber," *Construction and Building Materials*, vol. 122, pp. 628–636, 2016.

[14] A. Mcisaac and A. Fam, "Durability under freeze-thaw cycles of concrete beams retrofitted with externally bonded FRPs using bio-based resins," *Construction and Building Materials*, vol. 168, pp. 244–256, 2018.

[15] J. A. Bogas, J. de Brito, and D. Ramos, "Freeze-thaw resistance of concrete produced with fine recycled concrete aggregates," *Journal of Cleaner Production*, vol. 115, pp. 294–306, 2016.

[16] A. Alsaif, S. A. Bernal, M. Guadagnini, and K. Pilakoutas, "Freeze-thaw resistance of steel fibre reinforced rubberised concrete," *Construction and Building Materials*, vol. 195, pp. 450–458, 2019.

[17] A. Richardson, K. Coventry, and J. Bacon, "Freeze/thaw durability of concrete with recycled demolition aggregate compared to virgin aggregate concrete," *Journal of Cleaner Production*, vol. 19, no. 2-3, pp. 272–277, 2011.

[18] V. Penttala and F. Al-Neshawy, "Stress and strain state of concrete during freezing and thawing cycles," *Cement and Concrete Research*, vol. 32, no. 9, pp. 1407–1420, 2002.

[19] H. Yu, H. Ma, and K. Yan, "An equation for determining freeze-thaw fatigue damage in concrete and a model for predicting the service life," *Construction and Building Materials*, vol. 137, pp. 104–116, 2017.

[20] G. W. Scherer, "Crystallization in pores," *Cement and Concrete Research*, vol. 29, no. 8, pp. 1347–1358, 1999.

[21] G. Fagerlund, "The significance of critical degree of saturation at freezing of pore and brittle materials," in *Proceedings of the Scholar CF, Durability of Concrete*, pp. 13–65, American Concrete Institute, Detroit, MI, USA, 1975.
[22] T. C. Powers, "A working hypothesis for further studies of frost resistance of concrete," *ACI Journal*, vol. 16, no. 4, pp. 245–272, 1945.
[23] T. C. Powers, "Freezing effects in concrete," *Durability of Concrete*, vol. 47, pp. 1–11, ACI Special Publication, Indianapolis, IN, USA, 1975.
[24] Y. Ma, H. Liu, and M. Zhang, "Effects of desert sand replacement rate and fly ash content on the compressive strength of concrete under low temperature," *Industrial Architecture*, vol. 50, no. 5, pp. 81–87+80, 2020, in Chinese.
[25] GB/T 50082-2009, *National Standard of the People's Republic of China, Standard Test Method for Long-Term Performance and Durability of Ordinary Concrete*, National Standard of the People's Republic of China, Beijing, China, 2009, in Chinese.
[26] CECS 02: 2005, *National Standard of the People's Republic of China, Technical Specification for Ultrasonic Rebound Comprehensive Method for Testing Concrete Strength*, National Standard of the People's Republic of China, Beijing, China, 2005, in Chinese.
[27] GB/T 50081-2016, *National Standard of the People's Republic of China, Standard Test Method for Mechanical Properties of OC*, National Standard of the People's Republic of China, Beijing, China, 2016, in Chinese.
[28] H. Shang, J. Ou, and Y. Song, "Theory and reliability analysis of freeze-thaw damage of concrete structures," *Engineering Mechanics*, vol. 28, no. 01, pp. 70–74, 2011.
[29] M. Molero, S. Aparicio, G. Al-Assadi, M. J. Casati, M. G. Hernández, and J. J. Anaya, "Evaluation of freeze-thaw damage in concrete by ultrasonic imaging," *NDT & E International*, vol. 52, pp. 86–94, 2012.
[30] T. Suzuki, H. Ogata, R. Takada, M. Aoki, and M. Ohtsu, "Use of acoustic emission and X-ray computed tomography for damage evaluation of freeze-thawed concrete," *Construction and Building Materials*, vol. 24, no. 12, pp. 2347–2352, 2010.
[31] Y. Wang, M. Zhang, P. Xu, and W. Jian, "Research on the fatigue damage characters of the cement soil under dynamic load," *Advanced Materials Research*, vol. 160, pp. 990–995, 2011.
[32] P. Lawrence, M. Cyr, and E. Ringot, "Mineral admixtures in mortars," *Cement and Concrete Research*, vol. 33, no. 12, pp. 1939–1947, 2003.
[33] M. Cyr, P. Lawrence, and E. Ringot, "Mineral admixtures in mortarsQuantification of the physical effects of inert materials on short-term hydration," *Cement and Concrete Research*, vol. 35, no. 4, pp. 719–730, 2005.
[34] M. Sagrin, *Stress-stain Relationship for Concrete and the Analysis of Structural Concrete Sections*, Solid Mechanics Division, University of Waterloo, Waterloo, Canada, 1971.
[35] E. Hognestad, N. W. Hanson, and D. McHenry, "Concrete stress distribution in ultimate strength design," *ACI Journal*, vol. 52, no. 4, pp. 455–479, 1955.
[36] Z. Guo, *Strength and Deformation of Concrete: Experimental Basis and Constitutive Relationship*, Tsinghua University Press, Beijing, China, 1997, in Chinese.
[37] Y. Huang, X. He, Q. Wang, and Y. Sun, "Mechanical properties of sea sand recycled aggregate concrete under axial compression," *Construction and Building Materials*, vol. 175, pp. 55–63, 2018.
[38] G. E. Pellissier and S. M. Purdy, *Stereology and Quantitative Metallography*, American Society for Testing and Materials, Philadelphia, PA, USA, 1971.